

Local bifurcation with spin-transfer torque in superparamagnetic tunnel junctions

Takuya Funatsu ¹, Shun Kanai ^{1,2,3,4✉}, Jun'ichi Ieda ⁵, Shunsuke Fukami^{1,4,6,7,8✉} & Hideo Ohno ^{1,4,6,7}

Modulation of the energy landscape by external perturbations governs various thermally-activated phenomena, described by the Arrhenius law. Thermal fluctuation of nanoscale magnetic tunnel junctions with spin-transfer torque (STT) shows promise for unconventional computing, whereas its rigorous representation, based on the Néel-Arrhenius law, has been controversial. In particular, the exponents for thermally-activated switching rate therein, have been inaccessible with conventional thermally-stable nanomagnets with decade-long retention time. Here we approach the Néel-Arrhenius law with STT utilising superparamagnetic tunnel junctions that have high sensitivity to external perturbations and determine the exponents through several independent measurements including homodyne-detected ferromagnetic resonance, nanosecond STT switching, and random telegraph noise. Furthermore, we show that the results are comprehensively described by a concept of local bifurcation observed in various physical systems. The findings demonstrate the capability of superparamagnetic tunnel junction as a useful tester for statistical physics as well as sophisticated engineering of probabilistic computing hardware with a rigorous mathematical foundation.

¹Laboratory for Nanoelectronics and Spintronics, Research Institute of Electrical Communication, Tohoku University, Sendai, Japan. ²PRESTO, Japan Science and Technology Agency, Kawaguchi, Japan. ³Division for the Establishment of Frontier Sciences, Tohoku University, Sendai, Japan. ⁴Center for Science and Innovation in Spintronics, Tohoku University, Sendai, Japan. ⁵Advanced Science Research Center, Japan Atomic Energy Agency, Tokai, Japan. ⁶WPI-Advanced Institute for Materials Research, Tohoku University, Sendai, Japan. ⁷Center for Innovative Integrated Electronic Systems, Tohoku University, Sendai, Japan. ⁸Inamori Research Institute for Science, Kyoto, Japan. ✉email: skanai@tohoku.ac.jp; s-fukami@tohoku.ac.jp

A dynamical system is classified by the stability of its potential landscape, especially by the local bifurcation of the dynamical equation. Under finite stochasticity, the Arrhenius law, a general principle for thermally-activated events, describes a variety of dynamical phenomena ranging from chemical reactions to physical processes. According to the Arrhenius law, the relaxation time τ in staying at a certain state is given by $\tau = \tau_0 \exp\Delta$ with the thermal stability factor $\Delta \equiv E_0/k_B T$, where τ_0 is the intrinsic time constant of each system, k_B the Boltzmann constant, T the absolute temperature, and E_0 an intrinsic energy barrier for switching to different states without perturbation. Under the perturbation by normalised external input x , E_0 is replaced by an effective energy barrier $E = E_0(1-x)^{n_x}$, where the switching exponent n_x is determined by the effective energy landscape with x . In general, when the dynamical equation $d\Theta/dt = f(\Theta, x)$ is given, where t is the time and Θ is the state variable (e.g. particle position, spin quantisation direction, amount of unreacted substance, etc.), the types of local bifurcation of $f(\Theta, x)$ determines n_x ; for example, $n_x = 2$ for the pitchfork bifurcation and $n_x = 3/2$ for the saddle-node bifurcation¹. This suggests that the switching exponent serves as a unique lens for the local structure, especially the stability of the energy landscape under the perturbations in the relevant system.

In magnetic materials, which have served as a model system to study the physics of thermally-activated phenomena, the basis of the Arrhenius law was built by Néel² and Brown³, known as the Néel–Arrhenius law. For single-domain uniaxial magnets with a magnetic field H applied along the easy axis, E under magnetic field can be simply derived as $E = E_0(1 - H/H_K^{\text{eff}})^2$ by the Stoner–Wohlfarth model, where H_K^{eff} is the effective magnetic anisotropy field⁴. However, theoretical studies pointed out that the value of exponent n_H , 2 in the above equation, should vary when one considers some realistic factors such as misalignment of magnetic field^{5,6} and higher-order terms of anisotropy⁷; in other words, the local bifurcation varies with them.

The magnetisation of nanomagnets can also be controlled by spin-transfer torque (STT) under current application through the angular momentum transfer^{8–13}. The STT-induced magnetisation switching in thermally-stable magnetic tunnel junctions (MTJ) is a key ingredient for non-volatile magnetoresistive random access memory^{14–16}. Moreover, recent studies have demonstrated an unconventional paradigm of computing, e.g. neuromorphic computing with population coding¹⁷, and probabilistic computing¹⁸, which utilises a combinatorial effect of STT and thermal fluctuation in superparamagnetic tunnel junctions (s-MTJs). By further combining the effect of external magnetic fields, additional tunabilities of the s-MTJs for probabilistic computing have been shown¹⁹. In this regard, understanding how the effective energy of s-MTJs is characterised under STT, as well as magnetic field, is of significant interest not only from fundamental but also from technological aspects. The Néel–Arrhenius law under STT has been a long-standing question partly because the STT itself does not modulate the energy landscape due to its non-conservative nature, preventing one from defining its effective potential energy. Despite the difficulty, the expectation value of event time of the magnetisation switching, i.e. the Néel relaxation time τ , under field H and current I is phenomenologically expressed in a form:

$$\tau = \tau_0 \exp \left[\frac{E_0}{k_B T} \left(1 - \frac{H}{H_K^{\text{eff}}} \right)^{n_H} \left(1 - \frac{I}{I_{C0}} \right)^{n_I} \right], \quad (1)$$

where τ_0 is ~ 1 ns in magnetic systems³, and I_{C0} an intrinsic critical current. Regarding the exponent n_I for the factor of current, different values, 1 (refs. 20,21) or 2 (refs. 22–24), have been theoretically derived, where the former was obtained by considering a fictitious temperature, whereas the latter was obtained by analysing the stochastic process based on the Fokker–Planck equation.

Experimentally, it has been practically inaccessible as far as one examines conventional thermally-stable MTJs and consequently, their decade-long unperturbed retention property has been extrapolated from limited data obtained in a reasonable time while assuming a certain number for n_H or n_I ^{25–33}. For applications with superparamagnetic tunnel junctions that actively utilise thermal fluctuation under STT, such uncertainty makes sophisticated engineering impractical as a rigorous description of modulation of the effective energy landscape is indispensable.

Here we experimentally study the Néel–Arrhenius law of a nanomagnet under STT utilising superparamagnetic tunnel junctions that allow direct determination of the event time under fields and currents^{34–39}. Through measurements of homodyne-detected ferromagnetic resonance (FMR) under current biases, high-speed STT switching with various pulse widths, and random telegraph noise (RTN) under various fields and currents, values of n_H and n_I are uniquely determined for given conditions. Furthermore, we show that by considering the local bifurcations under magnetic field and STT, which have not been considered for magnetic systems, the obtained results can be comprehended with the effects of the torques of the field and current without the difficulties to define the effective potential of STT.

Sample preparation and strategy of following experiments

As shown in Fig. 1a, a stack structure, Ta(5)/Pt(5)/[Co(0.3)/Pt(0.4)]₇/Co(0.3)/Ru(0.45)/[Co(0.3)/Pt(0.4)]₂/Co(0.3)/Ta(0.3)/CoFeB/MgO(1.0)/CoFeB($t_{\text{CoFeB}} = 1.88$)/Ta(5)/Ru(5) (numbers in parenthesis are nominal thickness in nm), is deposited by dc/rf magnetron sputtering on a sapphire substrate. The stack possesses essentially the same structure as what was utilised in the demonstration of probabilistic computing¹⁸. Resistance (R)-area (A) product, RA , of the MgO tunnel barrier is $5.5 \Omega \mu\text{m}^2$. The stack is patterned into MTJ devices, followed by annealing at 300°C . The MTJ device we will mainly focus on hereafter (device A) has a diameter D of 34 nm (results for device B with $t_{\text{CoFeB}} = 1.82$ nm, $RA = 8.1 \Omega \mu\text{m}^2$, and $D = 28$ nm will be also shown later). In this size range, the magnetisation can be represented by a single vector without significant effects of spatial inhomogeneity for the present stack structure^{16,27,40}. Both CoFeB layers have a perpendicular easy axis. Figure 1b shows the junction resistance R as a function of the perpendicular magnetic field H_z . Gradual variation of mean R with H_z and scattering of data points at the transition region reflects a superparamagnetic nature of the MTJ whose switching time is shorter than the measurement time of R (~ 1 s).

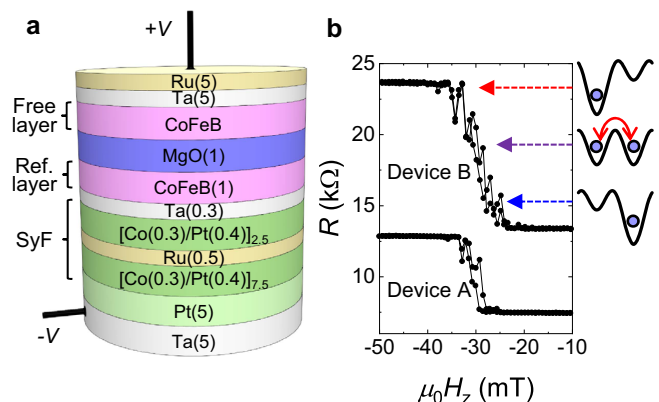


Fig. 1 Sample structure and R - H_z property. **a** Stack structure of the magnetic tunnel junction. **b** Resistance R as a function of external perpendicular magnetic field H_z .

To determine n_H and n_I in actual MTJs, we take into account the following two effects: electric-field modulation of magnetic anisotropy^{41–44} and uncompensated stray field H_S from the reference layer. Consequently, Δ , the argument of the exponential in Eq. (1), is rewritten as

$$\Delta_{P(AP)} = \frac{E_0}{k_B T} \left(1 \pm \frac{H_z - H_S}{H_K^{\text{eff}}(V)} \right)^{n_H} \left(1 - \frac{V}{V_{\text{CO,P(AP)}}} \right)^{n_I} \quad (2)$$

$$\equiv \Delta_0 (1 \pm h(H_z, V))^{n_H} (1 - v_{\text{P(AP)}}(V))^{n_I},$$

with $\Delta_0 \equiv E_0/k_B T$, $h(H_z, V) \equiv (H_z - H_S)/H_K^{\text{eff}}(V)$, and $v_{\text{P(AP)}}(V) \equiv V/V_{\text{CO,P(AP)}}$. $V_{\text{CO,P(AP)}}$ denotes the intrinsic critical voltage for STT switching from parallel, P, to antiparallel, AP,

states (AP to P states). Because the electric-field effect on anisotropy is governed by the applied voltage V , we use an expression based on voltage input rather than current input. Equation (2) contains so many unknown variables (E_0 , H_S , $H_K^{\text{eff}}(V)$, $V_{\text{CO,P(AP)}}$, n_H and n_I) that one cannot directly determine the exponents by only measuring RTN. Thus, in the following, we first separately determine $H_K^{\text{eff}}(V)$ from a homodyne-detected FMR and the next V_{CO} from the STT switching probability. After that, we determine H_S and the exponents n_H and n_I from RTN measurement^{34–38} as a function of V .

Electric-field effect on anisotropy field

Firstly, we determine $H_K^{\text{eff}}(V)$ from homodyne-detected FMR under dc bias voltage^{45,46}. Figure 2a shows the circuit configuration for the measurement. Homodyne-detected voltage spectra are measured while sweeping H_z at various frequencies and H_K^{eff} is determined from the peak position (see Methods and Supplementary Information for details). We perform this measurement at various dc biases and obtain H_K^{eff} vs. V , as shown in Fig. 2b. H_K^{eff} changes nonlinearly with V . We fit a quadratic equation to the obtained dependence and determine the coefficients for constant, linear, and quadratic terms to be $\mu_0 H_K^{\text{eff}}(0) = 77.0 \pm 0.5$ mT, $\mu_0 dH_K^{\text{eff}}/dV = -57.8 \pm 1.6$ mT V⁻¹, and $\mu_0 d^2H_K^{\text{eff}}/dV^2 = -49.9 \pm 7.5$ mT V⁻² (μ_0 is the permeability of vacuum). Note that the constant term represents the magnetic anisotropy field at zero bias whereas the linear and quadratic terms mainly originate from the electric-field modulation of anisotropy and an effect of Joule heating, respectively. The determined coefficients will be used in the analysis of RTN later.

Intrinsic critical voltage for STT switching

Secondly, we determine V_{CO} for the STT switching. Because the fluctuation timescale of the studied system is on the order of milliseconds, we need to measure the junction state right after the switching pulse application when they are still non-volatile. To this end, we use a circuit configuration shown in Fig. 3a. This configuration is similar to that we used in our previous work to

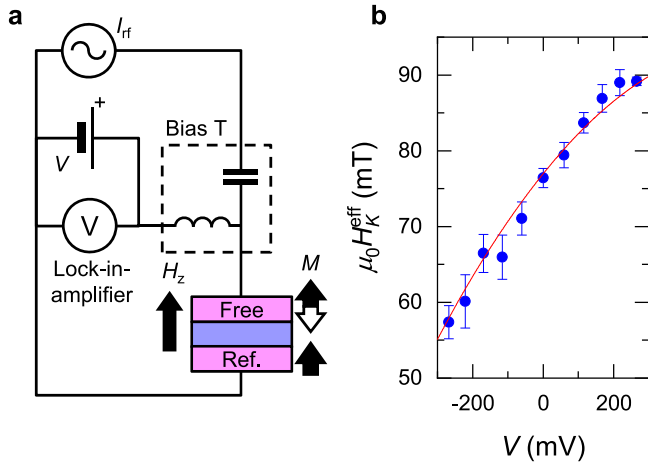


Fig. 2 Homodyne-detected ferromagnetic resonance. **a** Electrical circuit for homodyne-detected ferromagnetic resonance (FMR). **b** DC bias voltage V dependence of effective anisotropy field ($\mu_0 H_K^{\text{eff}}$) determined by FMR. Red curves are fitting with a quadratic function to the plots. The error bar shows the standard error of fitting Kittel’s resonant condition to the experimentally obtained resonant frequency versus perpendicular magnetic field H_z .

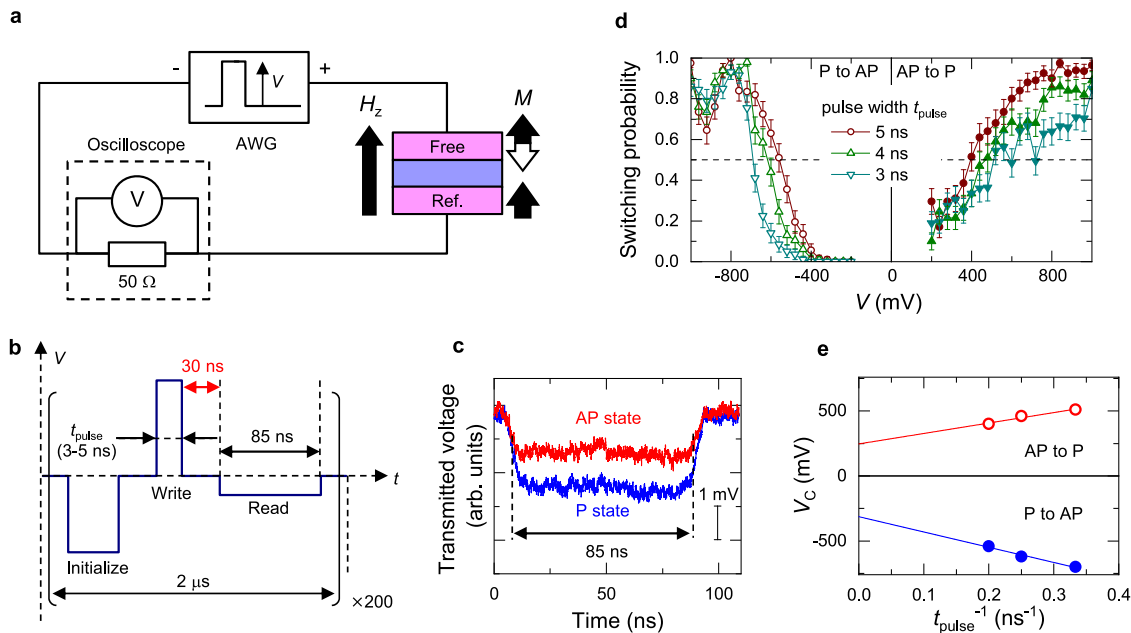


Fig. 3 Spin-transfer torque switching. **a** Circuit configuration to measure spin-transfer-torque (STT) switching probability of low thermal stability factor MTJs. **b** Schematics of voltage waveform applied to MTJs. **c** Transmitted voltage monitored at oscilloscope during read sequence with a duration of 85 ns. **d** Switching probability as a function of pulse voltage amplitude V with different write pulse duration t_{pulse} . **e** Switching voltage V_C as a function of t_{pulse}^{-1} . Lines are linear fits, whose intercept yields intrinsic critical voltages $V_{\text{CO,P(AP)}}$.

study the switching error rate⁴⁷; a voltage waveform composed of initialisation, write, and read pulses [Fig. 3b] is applied to the MTJ by an arbitrary waveform generator, and the transmitted signal at the read pulse is monitored by a high-speed oscilloscope to identify the final state of magnetisation configuration. The typical transmitted signals for P and AP states are shown in Fig. 3c. A clear difference is observed in the amplitude of the transmitted signal for different configurations due to the tunnel magnetoresistance. Write and read pulses are separated by 30 ns, which is much shorter than the shortest relaxation time shown later (~ 0.3 ms), ensuring a sufficiently low read-error rate (unintentional switching probability before the read pulse) $< 10^{-4}$ (see Methods). The waveform is applied 200 times repeatedly and switching probability is evaluated.

Figure 3d shows the write pulse voltage dependence of the switching probability with different write pulse durations t_{pulse} . The switching voltage V_C , defined as the voltage at 50% probability, is plotted as a function of the inverse of t_{pulse} in Fig. 3e. In the precessional regime (typically $t_{\text{pulse}} \lesssim$ several nanoseconds) where the switching/non-switching is determined by an amount of transferred angular momenta, V_C is known to linearly depend on t_{pulse}^{-1} and the intercept yields V_{CO} ^{20,48}. From a linear fitting, $V_{\text{CO,P}}$ and $V_{\text{CO,AP}}$ are obtained as 313 ± 45 mV and -247 ± 42 mV, respectively.

Random telegraph noise measurement to determine the switching exponents

With the results above, we are now ready to determine the switching exponents, n_H and n_b , from RTN measurement under various V and H_z . Figures 4a, b show the circuit configurations for the measurement with $V \sim 0$ and $|V| \geq 25$ mV, respectively. For $V \sim 0$, we apply a small direct current $I = 200$ nA and

monitor R by an oscilloscope connected in parallel to the MTJ and probe the temporal magnetisation configuration. For $|V| \geq 25$ mV, we monitor the divided voltage at reference resistor R_r serially connected to the MTJ using an oscilloscope. Note that $R_r (= 470 \Omega)$ is set to be much smaller than R to prevent a change in the electric-field effect on the magnetic anisotropy between P and AP states. Figure 4c shows typical results of RTN with various H_z and the definition of the magnetisation switching event time t . Figure 4d shows the distribution of the number of unique t for $\mu_0 H_z = -30.5$ mT. As expected, the exponential distribution is confirmed, i.e., the number of events $\propto \tau^{-1} \exp(-t/\tau)$, indicating that the fluctuation is characterised by a Poisson process. From the fitting, expectation values of the event time for P and AP states, i.e., the relaxation time τ_P and τ_{AP} , are obtained as a function of H_z as shown in Fig. 4e. Subsequently, $\Delta_{\text{P(AP)}}$ can be determined from the relation $\tau = \tau_0 \exp(\Delta_{\text{P(AP)}}$.

We measure $\tau_{\text{P(AP)}}$ and $\Delta_{\text{P(AP)}}$ for various H_z and V . Figure 5a shows the obtained Δ_P and Δ_{AP} as a function of H_z for various V . $\Delta_{\text{P(AP)}}$ increases (decreases) with increasing H_z for each V , as expected from the energy landscape modulation by H_z . Also, the mean Δ gradually decreases with increasing V , which is also consistent with the trend of H_K^{eff} shown in Fig. 2b. To derive n_H and n_b , we then take the natural logarithm of the ratio between Δ_P and Δ_{AP} , which can be expressed from Eq. (2) as

$$\ln \frac{\Delta_P}{\Delta_{\text{AP}}} = n_H \ln \frac{1+h}{1-h} + n_b \ln \frac{1-v_P}{1-v_{\text{AP}}} \quad (3)$$

$\ln(\Delta_P/\Delta_{\text{AP}})$ vs. H_z for each V is plotted in Fig. 5b. At a small perturbation limit, i.e., $h, v_P, v_{\text{AP}} \ll 1$, Eq. (3) is reduced to $\ln(\Delta_P/\Delta_{\text{AP}}) = 2n_H h + n_b(v_{\text{AP}} - v_P)$; thus, the slope and intercept of the linear fit to the data shown in Fig. 5b give n_H and n_b ,

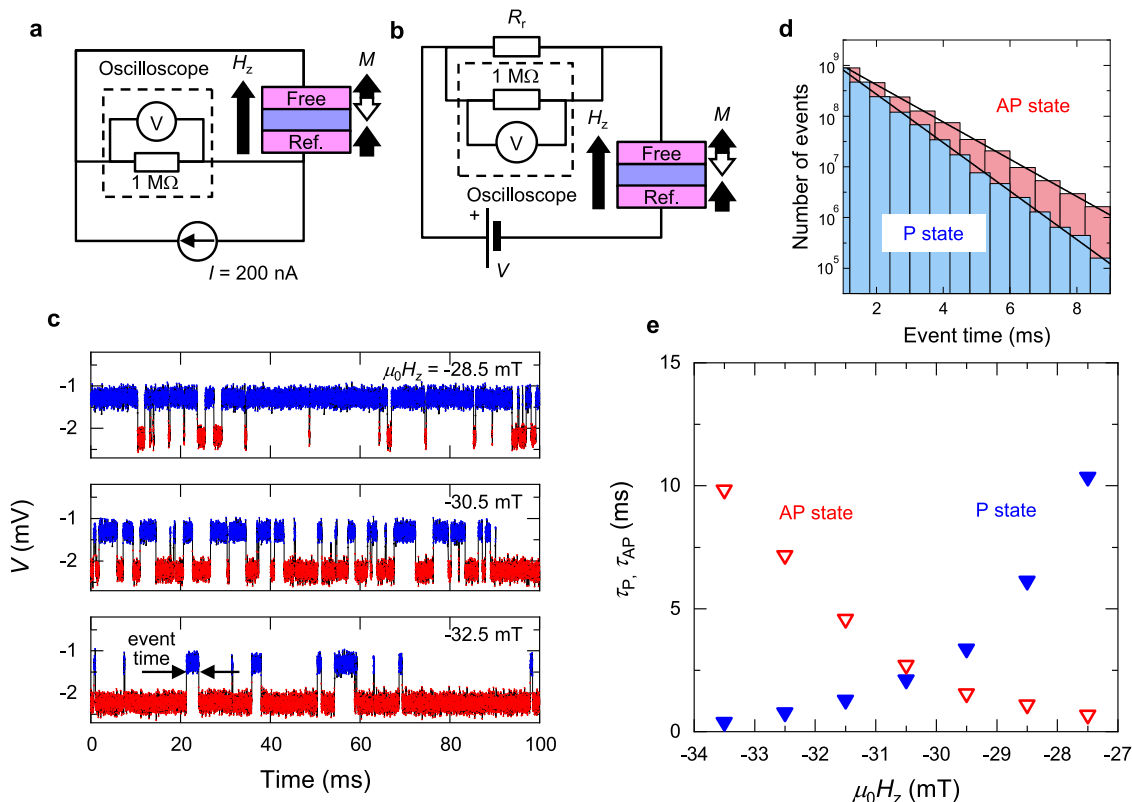


Fig. 4 Random telegraph noise. **a, b** Circuit configuration to measure random telegraph noise (RTN) with $V \sim 0$ and $V \geq 25$ mV, respectively. **c** Typical RTN signal monitored at the oscilloscope. **d** Histogram of event time (duration between two sequential switching events) for P and AP states for $\mu_0 H_z = -30.5$ mT. **e** Expected switching time as a function of perpendicular magnetic field H_z .

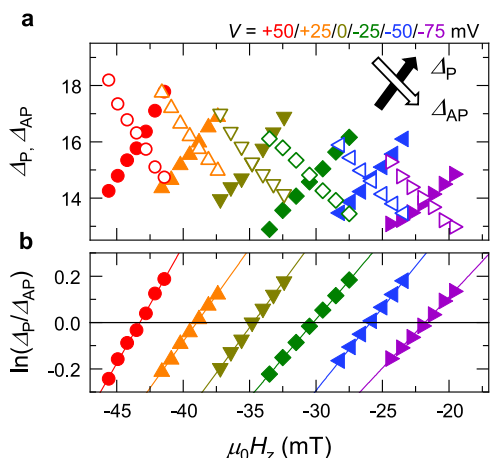


Fig. 5 Δ_P , Δ_{AP} , and their ratio. **a** Thermal stability factors for P and AP states Δ_P and Δ_{AP} are determined by RTN measurement. **b** Natural log of their ratio as functions of perpendicular magnetic field H_z and V .

respectively. One can see that the results are well fitted by the linear function, validating the employed model.

We analyse Fig. 5 with Eq. (3) and obtain n_H and n_I as a function of V for device A as shown in Fig. 6a. One can see that both n_H and n_I show similar values at each V and gradually decreases to about 1.5 with decreasing V . We perform the same procedure for the device B, whose properties are determined as $\mu_0 H_K^{\text{eff}}(0) = 129.0 \pm 0.7$ mT, $\mu_0 dH_K^{\text{eff}}/dV = -61.7 \pm 2.3$ mT V⁻¹, $\mu_0 d^2H_K^{\text{eff}}/dV^2 = -58 \pm 13$ mT V⁻², $V_{\text{Co,P}} = 672 \pm 4$ mV and $V_{\text{Co,AP}} = -541 \pm 2$ mV. The obtained n_H and n_I are shown in Fig. 6b. At $V = 0$, the two devices show the same value for n_H within experimental inaccuracy. Also, both n_H and n_I of device B show similar values with each other as in device A. However, in contrast to device A, they do not show meaningful variations at around 2 with V .

Discussion

As shown above, we have found that n_H and n_I show virtually the same value with each other for both devices A and B. Also, they are almost constant at around 2.0 for device B whereas change from 2.0 to 1.5 with V for device A. The main difference between devices A and B is t_{CoFeB} , which manifests in a difference in $\mu_0 H_K^{\text{eff}}(0)$ [77.0 \pm 0.5 mT for device A and 129.0 \pm 0.7 mT for device B]. In the following, we will discuss the mechanism that can account for the obtained results in the context of the energy landscape and its bifurcation.

In systems with uniaxial anisotropy where the magnetic field is applied along the easy axis where the macrospin approximation holds, Brown derived $n_H = 2$ in a high barrier region, $E_0 \gtrsim k_B T$, using Kramers' analysis on the Fokker–Planck equation that is equivalent to the Landau–Lifshitz–Gilbert (LLG) equation with the Langevin term³. Taking into consideration the second-order anisotropy, where the magnetic anisotropy energy density is given by $\mathcal{E} = K_1^{\text{eff}} \sin^2 \theta + K_2 \sin^4 \theta$, n_H was pointed out to vary with K_2/K_1^{eff} ⁷, where K_1^{eff} , K_2 and θ are the first- and second-order effective anisotropy fields and polar angle of magnetisation vector, respectively. In the CoFeB/MgO system, positive voltage, which decreases electron density at the interface, was found to increase K_1^{eff} , while keeping $\mu_0 H_{K2} (\equiv \mu_0 K_2/4M_S)$ constant at around 45 mT^{46,49,50}. Accordingly, as shown in the upper axes of Fig. 6a, b, in the present cases, K_2/K_1^{eff} is calculated to be around 0.22 for device B whereas it increases up to 0.45 for device A. The numerical calculation, assuming material parameters of magnetic

recording media ($\Delta_0 \gtrsim 60$), shows that n_H decreases from 2.0 to 1.5 in the range of K_2/K_1^{eff} from 0 to 0.25⁷. In general, a dynamical system with pitchfork bifurcation leads to the switching exponent of $n_x = 2$, while saddle-node bifurcation results in $n_x = 3/2$. Note that the aforementioned magnetic energy density \mathcal{E} gives the LLG equation $d\theta/dt = f(\theta, H_z) = -\alpha\gamma\mu_0[(2K_1^{\text{eff}}/M_S)\cos\theta - (4K_2/M_S)\cos^3\theta - H_z]\sin\theta$. We show $f(\theta, H_z)$ takes two types of local bifurcations: pitchfork bifurcation appears at $K_2/K_1^{\text{eff}} < 0.25$, while saddle-node bifurcation at $K_2/K_1^{\text{eff}} > 0.25$ as shown in Fig. 6c, d, respectively [see Supplementary Information in detail]. Thus, the experimentally observed transition of the switching exponents is attributed to the transition of the bifurcation of the potential landscape through the modulation of K_2/K_1^{eff} . However, the experiment shows the transition of n_H at $K_2/K_1^{\text{eff}} \approx 0.45$, which is larger than that expected by the macrospin model ($K_2/K_1^{\text{eff}} = 0.25$). This deviation implies that the local bifurcation of the magnetic potential and the resultant n_H in the real MTJ device is more insensitive to higher-order anisotropy field K_2 than the macrospin limit, for example, due to the micromagnetic effects.

Regarding n_I , some theoretical studies derived 1 by considering a fictitious temperature in LLG equation with the Langevin term^{20,21}, whereas others derived 2 from an analysis of the Fokker–Planck equation^{22–24}. Matsumoto et al. pointed out that n_I rapidly decreases from 2 to 1.4 with increasing K_2/K_1^{eff} from 0 to ~ 0.25 ⁵¹. Experimentally, some assumed 1^{25,27–30,36,39} whereas others assumed 2^{26,31–33}, and importantly no studies access the number. The present experimental results support the scenario of Matsumoto et al., but, similarly to n_H , the reduction of n_I is more moderate than the theoretical prediction. This fact indicates that the mechanism for n_H could be also applicable for the case with STT perturbation as well. Another important implication of our results is that, despite the non-conservative nature of STT, the pseudo energy landscape under STT can be investigated through the switching exponents. LLG equation with STT τ_{STT} can be represented as $d\theta/dt = f(\theta, x) = \{-\alpha\gamma\mu_0[(2K_1^{\text{eff}}/M_S)\cos\theta - (4K_2/M_S)\cos^3\theta] + \tau_{\text{STT}}\}\sin\theta$. Since n_H and n_I show virtually the same value for all K_2/K_1^{eff} conditions, meaning that $f(\theta, \tau_{\text{STT}})$ takes the same local bifurcation type as that for $f(\theta, H)$, our experiment reveals that in MTJ devices with perpendicular easy axis, the magnetic field and the STT effectively similarly modulate the energy landscape.

In summary, this work has experimentally revealed the hitherto-inaccessible representation of thermally-activated switching rate under field and STT, using a relevant material system for applications. The obtained results could allow for sophisticated engineering of non-volatile memory and unconventional computing hardware. Through the switching exponents, we have also accessed the local bifurcation of energy landscape under STT, and have found that, despite the qualitative difference between magnetic field and STT, their effect on the energy landscape is equivalent in the case of perpendicular MTJ. This work has also demonstrated that superparamagnetic tunnel junctions and analysis of their local bifurcation can serve as a versatile tool to investigate unexplored physics relating to thermally-activated phenomena in general with various configurations and external perturbations.

Methods

Sample preparation. Stacks with Ta(5)/Pt(5)/[Co(0.3)/Pt(0.4)]_n/Co(0.3)/Ru(0.45)/[Co(0.3)/Pt(0.4)]₂/Co(0.3)/Ta(0.3)/CoFeB(1.0)/MgO(1.0)/CoFeB(t_{CoFeB})/Ta(5)/Ru(5) (numbers in parenthesis are thickness in nm) were deposited by dc/rf magnetron sputtering on a sapphire substrate. The nominal CoFeB thicknesses $t_{\text{CoFeB}} = 1.88$ nm (device A) and 1.82 nm (device B). After the deposition, the stacks were processed into MTJs by a hard-mask process with electron-beam lithography, followed by annealing at 300 °C under a perpendicular magnetic field of 0.4 T for 1 h. The resistance (R)-area (A) product (RA) was determined from the physical

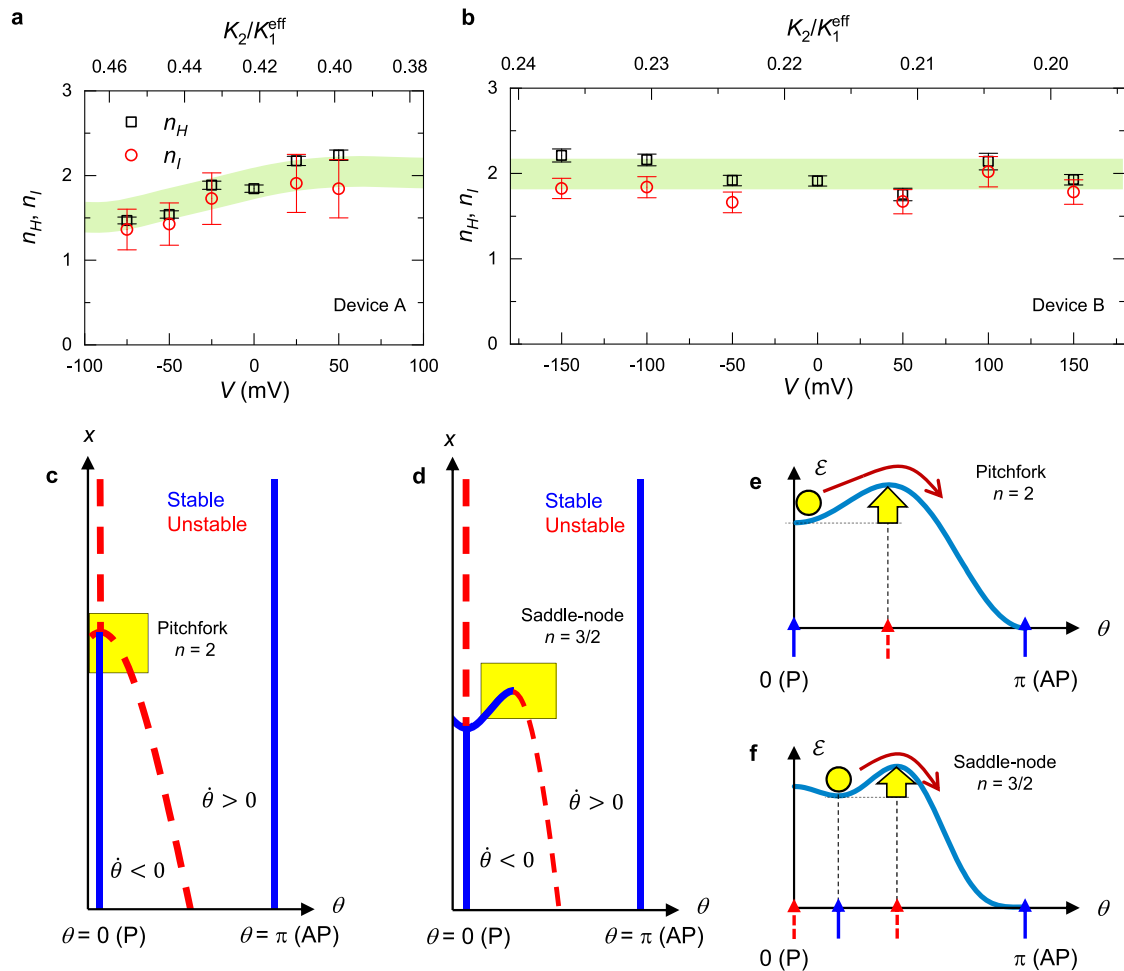


Fig. 6 Experimentally determined switching exponents n_H , n_I . **a**, **b** Field- and current-induced switching exponents n_H and n_I as a function of bias voltage V for **a** device A and **b** device B. Error bars show standard error propagated from ferromagnetic resonance measurement and critical current measurement. The green band is a guide to the eye. **c**, **d** Bifurcation diagrams of the $d\theta/dt$ projected upon $(\theta, x) = (\theta, H)$ or (θ, I) for **c** $K_2/K_1^{\text{eff}} < 0.25$ and **d** $K_2/K_1^{\text{eff}} > 0.25$, where K_1^{eff} , K_2 , θ , t , H , and I are the first- and second-order effective anisotropy fields, polar angle of magnetisation vector, the time, perpendicular magnetic field, and current. **e**, **f** Schematics of energy barrier of the effective magnetic potential corresponding to the yellow region in **c** and **d**, respectively.

size determined from scanning electron microscopy observation and measured resistance for large devices with diameter $D > 45$ nm. The resistance-area product of device A (device B) is $5.5 \Omega \mu\text{m}^2$ ($8.1 \Omega \mu\text{m}^2$), and the tunnel magnetoresistance ratio is 73% (74%). The nominal thickness of the MgO is 1.0 nm for both devices, and the difference of the RA corresponds to the $\sim 7\%$ variation of the actual thickness due to the process variations between the two runs. D of devices A and B are determined from their resistance and RA to be $D = 34$ and 28 nm, respectively.

Homodyne-detected ferromagnetic resonance (FMR). With the circuit shown in Fig. 2a, homodyne-detected voltage- H_z spectra were measured at various frequencies. As shown in previous papers, the spectra were well fitted by the Lorentz function and peak position was determined by the fitting^{45,46}. From resonance frequency f_r vs. H_z , the effective anisotropy field H_K^{eff} was determined while assuming a constant second-order anisotropy field $\mu_0 H_{K2} = 45$ mT^{46,49,50} (μ_0 is the permeability of vacuum). The measurement was performed at various dc biases at AP configuration and obtained H_K^{eff} vs. V , as shown in Fig. 2b. A quadratic equation was fitted to the obtained dependence and the coefficients for constant, linear and quadratic terms were determined. Note that, in the error of H_K^{eff} , we have included the effect of H_K^{eff} difference in P and AP configurations due to the different device resistances and resultant Joule heatings in these configurations under the identical bias voltage.

Switching probability measurement. With the circuit shown in Fig. 3a, the switching probability was measured as functions of write pulse voltage amplitude and duration to determine intrinsic critical voltage V_{CO} . A voltage waveform composed of initialisation (0.45 V/300 ns), write (amplitude V_{write} /duration t_{pulse}), and read ($V_{\text{read}} = 0.15$ V/75 ns) pulses as shown in Fig. 3b, was generated by an arbitrary waveform generator (AWG). Both the interval of initialisation/write and write/read

pulses were 30 ns, which is much shorter than the shortest relaxation time measured here (~ 0.3 ms), ensuring a sufficiently low read-error rate due to unintentional switching probability before the read pulse, $\exp(-30 \text{ ns}/0.3 \text{ ms}) \leq 10^{-4}$. Single-shot-transmitted voltage for write pulse was monitored to determine the magnetisation configuration; the transmitted voltage is $\sim 2Z_0 V_{\text{read}}/(R + Z_0)$, where Z_0 is characteristic impedance 50Ω , and due to the tunnel magnetoresistance, the transmitted voltage changes with magnetisation configuration. The typical transmitted signal for P and AP states is shown in Fig. 3c. Transmitted signals for 5 ns (between 15 and 20 ns in Fig. 3c) were averaged. Its averaged value $\langle V \rangle$ and standard error $\langle (V - \langle V \rangle)^2 \rangle^{0.5}/N^{0.5}$ for P and AP states were 2.44 ± 0.03 mV and 1.40 ± 0.03 mV, respectively (N is averaged points; 20 Gbit/s \times 5 ns duration = 100 points), ensuring low read-error rate due to misassignment of the magnetisation configuration⁴⁷. As shown in Fig. 3d, switching probability as a function of the voltage amplitude V at MTJ with write pulse duration t_{pulse} from 1 to 5 ns was measured. The probability of the switching was determined from 200 times measurement. The switching measurement was conducted under H_z of the stray field H_S which was determined from the random telegraph noise measurement. Note that the anomaly of the switching probability at $V \sim -900$ mV can be attributed to a change of the magnetic easy axis through the electric-field effect on the magnetic anisotropy, which is reported in previous works⁵². In addition, the slope of the switching probability at $P_{\text{sw}} \sim 0.5$ for P to AP switching increases with decreasing the pulse duration, which is opposite to the thermally-stable MTJs. The decreases of the effective field and the thermal stability factor through the electric-field effect on magnetic anisotropy reasonably explain the behaviour.

Random telegraph noise (RTN). With the circuit shown in Fig. 4a, the RTN signal of the MTJs for $V \sim 0$ was measured. Small direct current $I = 200$ nA was applied and R was monitored by an oscilloscope connected in parallel to the MTJ to probe the temporal magnetisation configuration. The voltage applied to MTJ here was up to 2.5 mV

(5 mV) for device A (device B), which is small enough to prevent major voltage/current-induced effects in MTJs focused here. If one utilises the same circuit, the applied voltage for P and AP states varies by a factor of about 1.7 due to the tunnel magnetoresistance effect. Therefore, to prevent variation of effective anisotropy field for P and AP states, the circuit shown in Fig. 4b was utilised for $|V| \geq 25$ mV. Direct voltage V to the MTJ was applied and divided voltage at reference resistor R_r connected in serial to the MTJ was monitored using the oscilloscope. For measuring RTN on device A (device B), with setting $R_r = 0.47$ k Ω (1 k Ω) much smaller than R , variation of applied voltages between P and AP states was prevented.

Attempt frequency. In determining Δ with the random telegraph noise measurement, Néel–Arrhenius law $\tau_{P(AP)} = \tau_0 \exp(\Delta_{P(AP)})$ with attempt frequency τ_0 of 1 ns was assumed. This assumption is widely adopted because τ is an exponential function of Δ and the value of τ_0 does not affect the estimated Δ , and τ_0 ranges between 0.1 and 10 ns. According to Brown's calculation with Kramer's method on the Fokker–Planck equation³, the attempt frequency τ_0 of the magnetic materials with uniaxial perpendicular magnetic anisotropy is $2\alpha\gamma\mu_0 H_K \text{eff} (1-h^2)(1+h)^{-1} (\pi/\Delta_0)^{0.5}$ under large barrier approximation $\Delta_0 \gg 1$, where α , γ , and μ_0 are damping constant 0.006, gyromagnetic ratio, and permeability of vacuum, respectively. In our devices, the Brown's attempt frequency above is derived to be 1.1 and 2.4 ns for device A and device B, respectively. Thus, the switching time τ vs. thermal stability factor Δ of device A should be well described by the Néel–Arrhenius law with $\tau_0 = 1$ ns.

Data availability

The data that support the plots within this paper have been deposited in Zenodo at <https://zenodo.org/record/6767828>³³.

Received: 20 October 2021; Accepted: 4 July 2022;

Published online: 14 July 2022

References

- Strogatz, S. H. *Nonlinear Dynamics and Chaos: With Applications to Physics, Biology, Chemistry, and Engineering (Studies in Nonlinearity)* (CRC Press, 2001).
- Néel, L. Theorie du tramage magnetique des ferromagnetiques en grains fins avec application aux terres cuites. *Ann. Geophys.* **5**, 99–136 (1949).
- Brown, W. F. Thermal fluctuations of a single-domain particle. *Phys. Rev.* **130**, 1677–1686 (1963).
- Stoner, E. C. & Wohlfarth, E. P. A mechanism of magnetic hysteresis in heterogeneous alloys. *Philos. Trans. R. Soc. A* **240**, 599–642 (1948).
- Victoria, R. H. Predicted time dependence of the switching field for magnetic materials. *Phys. Rev. Lett.* **63**, 457–460 (1989).
- Tannous, C. & Gieraltowski, J. The Stoner–Wohlfarth model of ferromagnetism. *Eur. J. Phys.* **29**, 475–487 (2008).
- Kitakami, O., Shimatsu, T., Okamoto, S., Shimada, Y. & Aoi, H. Sharrock relation for perpendicular recording media with higher-order magnetic anisotropy terms. *Jpn. J. Appl. Phys.* **43**, L115–L117 (2004).
- Slonczewski, J. C. Current-driven excitation of magnetic multilayers. *J. Magn. Magn. Mater.* **159**, L1–L7 (1996).
- Berger, L. Emission of spin waves by a magnetic multilayer traversed by a current. *Phys. Rev. B* **54**, 9353–9358 (1996).
- Tsoi, M. et al. Excitation of a magnetic multilayer by an electric current. *Phys. Rev. Lett.* **80**, 4281–4284 (1998).
- Myers, E. B., Ralph, D. C., Katine, J. A., Louie, R. N. & Buhrman, R. A. Current-induced switching of domains in magnetic multilayer devices. *Science* **285**, 867–870 (1999).
- Katine, J. A., Albert, F. J., Buhrman, R. A., Myers, E. B. & Ralph, D. C. Current-driven magnetization reversal and spin-wave excitations in Co/Cu/Co pillars. *Phys. Rev. Lett.* **84**, 3149–3152 (2000).
- Brataas, A., Kent, A. D. & Ohno, H. Current-induced torques in magnetic materials. *Nat. Mater.* **11**, 372–381 (2012).
- Kent, A. D. & Worledge, D. C. A new spin on magnetic memories. *Nat. Nanotechnol.* **10**, 187–191 (2015).
- Apalkov, D., Dieny, B. & Slaughter, J. M. Magnetoresistive random access memory. *Proc. IEEE* **104**, 1796–1830 (2016).
- Jinnai, B., Watanabe, K., Fukami, S. & Ohno, H. Scaling magnetic tunnel junction down to single-digit nanometers—Challenges and prospects. *Appl. Phys. Lett.* **116**, 160501 (2020).
- Mizrahi, A. et al. Neural-like computing with populations of superparamagnetic basis functions. *Nat. Commun.* **9**, 1533 (2018).
- Borders, W. A. et al. Integer factorization using stochastic magnetic tunnel junctions. *Nature* **573**, 390–393 (2019).
- Lv, Y., Bloom, R. P. & Wang, J. Experimental demonstration of probabilistic spin logic by magnetic tunnel junctions. *IEEE Magn. Lett.* **10**, 4510905 (2019).
- Koch, R. H., Katine, J. A. & Sun, J. Z. Time-resolved reversal of spin-transfer switching in a nanomagnet. *Phys. Rev. Lett.* **92**, 088302 (2004).
- Li, Z. & Zhang, S. Thermally assisted magnetization reversal in the presence of a spin-transfer torque. *Phys. Rev. B* **69**, 134416 (2004).
- Taniguchi, T. & Imamura, H. Thermally assisted spin transfer torque switching in synthetic free layers. *Phys. Rev. B* **83**, 054432 (2011).
- Butler, W. H. et al. Switching distributions for perpendicular spin-torque devices within the macrospin approximation. *IEEE Trans. Magn.* **48**, 4684–4700 (2012).
- Pinna, D., Mitra, A., Stein, D. L. & Kent, A. D. Thermally assisted spin-transfer torque magnetization reversal in uniaxial nanomagnets. *Appl. Phys. Lett.* **101**, 262401 (2012).
- Fuchs, G. D. et al. Adjustable spin torque in magnetic tunnel junctions with two fixed layers. *Appl. Phys. Lett.* **86**, 152509 (2005).
- Sato, H. et al. Perpendicular-anisotropy CoFeB–MgO magnetic tunnel junctions with a MgO/CoFeB/Ta/CoFeB/MgO recording structure. *Appl. Phys. Lett.* **101**, 022414 (2012).
- Thomas, L. et al. Perpendicular spin transfer torque magnetic random access memories with high spin torque efficiency and thermal stability for embedded applications (invited). *J. Appl. Phys.* **115**, 172615 (2014).
- Zhao, H. et al. Low writing energy and sub nanosecond spin torque transfer switching of in-plane magnetic tunnel junction for spin torque transfer random access memory. *J. Appl. Phys.* **109**, 07c720 (2011).
- Heindl, R., Rippard, W. H., Russek, S. E., Pufall, M. R. & Kos, A. B. Validity of the thermal activation model for spin-transfer torque switching in magnetic tunnel junctions. *J. Appl. Phys.* **109**, 073910 (2011).
- Sukegawa, H. et al. Spin-transfer switching in full-Heusler Co2FeAl-based magnetic tunnel junctions. *Appl. Phys. Lett.* **100**, 182403 (2012).
- Nakayama, M. et al. Spin transfer switching in TbCoFe/CoFeB/MgO/CoFeB/TbCoFe magnetic tunnel junctions with perpendicular magnetic anisotropy. *J. Appl. Phys.* **103**, 07A710 (2008).
- Van Beek, S. et al. Thermal stability analysis and modelling of advanced perpendicular magnetic tunnel junctions. *AIP Adv.* **8**, 055909 (2018).
- Lourembam, J., Chen, B. J., Huang, A. H., Allauddin, S. & Ter Lim, S. A non-collinear double MgO based perpendicular magnetic tunnel junction. *Appl. Phys. Lett.* **113**, 022403 (2018).
- Urazhdin, S., Birge, N. O., Pratt, W. P. Jr. & Bass, J. Current-driven magnetic excitations in permalloy-based multilayer nanopillars. *Phys. Rev. Lett.* **91**, 146803 (2003).
- Wegrowe, J. E. Magnetization reversal and two-level fluctuations by spin injection in a ferromagnetic metallic layer. *Phys. Rev. B* **68**, 214414 (2003).
- Rippard, W., Heindl, R., Pufall, M., Russek, S. & Kos, A. Thermal relaxation rates of magnetic nanoparticles in the presence of magnetic fields and spin-transfer effects. *Phys. Rev. B* **84**, 064439 (2011).
- Chiba, D., Ono, T., Matsukura, F. & Ohno, H. Electric field control of thermal stability and magnetization switching in (Ga,Mn) As. *Appl. Phys. Lett.* **103**, 142418 (2013).
- Enobio, E. C. I., Bersweiler, M., Sato, H., Fukami, S. & Ohno, H. Evaluation of energy barrier of CoFeB/MgO magnetic tunnel junctions with perpendicular easy axis using retention time measurement. *Jpn. J. Appl. Phys.* **57**, 04FN08 (2018).
- Zink, B. R., Lv, Y. & Wang, J. P. Independent control of antiparallel- and parallel-state thermal stability factors in magnetic tunnel junctions for telegraphic signals with two degrees of tunability. *IEEE Trans. Electron Devices* **66**, 5353–5359 (2019).
- Sun, J. Z. et al. Spin-torque switching efficiency in CoFeB–MgO based tunnel junctions. *Phys. Rev. B* **88**, 104426 (2013).
- Chiba, D. et al. Magnetization vector manipulation by electric fields. *Nature* **455**, 515–518 (2008).
- Maruyama, T. et al. Large voltage-induced magnetic anisotropy change in a few atomic layers of iron. *Nat. Nanotechnol.* **4**, 158–161 (2009).
- Endo, M., Kanai, S., Ikeda, S., Matsukura, F. & Ohno, H. Electric-field effects on thickness dependent magnetic anisotropy of sputtered MgO/Co40Fe40B20/Ta structures. *Appl. Phys. Lett.* **96**, 212503 (2010).
- Kanai, S., Matsukura, F. & Ohno, H. Electric-field-induced magnetization switching in CoFeB/MgO magnetic tunnel junctions. *Jpn. J. Appl. Phys.* **56**, 0802A0803 (2017).
- Tulapurkar, A. A. et al. Spin-torque diode effect in magnetic tunnel junctions. *Nature* **438**, 339–342 (2005).
- Kanai, S., Gajek, M., Worledge, D. C., Matsukura, F. & Ohno, H. Electric field-induced ferromagnetic resonance in a CoFeB/MgO magnetic tunnel junction under dc bias voltages. *Appl. Phys. Lett.* **105**, 242409 (2014).
- Saino, T. et al. Write-error rate of nanoscale magnetic tunnel junctions in the precessional regime. *Appl. Phys. Lett.* **115**, 142406 (2019).
- Bedau, D. et al. Spin-transfer pulse switching: From the dynamic to the thermally activated regime. *Appl. Phys. Lett.* **97**, 262502 (2010).

49. Okada, A. et al. Electric-field effects on magnetic anisotropy and damping constant in Ta/CoFeB/MgO investigated by ferromagnetic resonance. *Appl. Phys. Lett.* **105**, 052415 (2014).
50. Okada, A., Kanai, S., Fukami, S., Sato, H. & Ohno, H. Electric-field effect on the easy cone angle of the easy-cone state in CoFeB/MgO investigated by ferromagnetic resonance. *Appl. Phys. Lett.* **112**, 172402 (2018).
51. Matsumoto, R., Arai, H., Yuasa, S. & Imamura, H. Efficiency of spin-transfer-torque switching and thermal-stability factor in a spin-valve nanopillar with first- and second-order uniaxial magnetic anisotropies. *Phys. Rev. Appl.* **7**, 044005 (2017).
52. Ohshima, N. et al. Current-induced magnetization switching in a nano-scale CoFeB-MgO magnetic tunnel junction under in-plane magnetic field. *AIP Adv.* **7**, 055927 (2017).
53. Funatsu, T. et al. Dataset: “local bifurcation with spin-transfer torque in superparamagnetic tunnel junctions.” *Zenodo*. <https://zenodo.org/record/6767828> (2022).

Acknowledgements

The authors thank O. Kitakami, M. Stiles, W. A. Borders and Y. Utsumi for fruitful discussion and B. Jinnai, H. Sato, K. Watanabe, J. Igarashi, M. Shinozaki, T. Saino, Z. Wang, T. Hirata, H. Iwanuma, I. Morita, R. Ono, S. Musya and C. Igarashi for technical supports. This work was partly supported by the ImPACT Programme of CSTI (S.F. and H.O.), JST-OPERA JPMJOP1611 (S.F. and H.O.), JST-CREST JPMJCR19K3 (S.F.), JST-PRESTO JPMJPR21B2 (S.K.), JSPS Core-to-Core Programme (S.K., S.F. and H.O.), JSPS Kakenhi 19H05622 (S.K., J.I. and S.F.), Shimadzu Research Foundation (S.K.), and RIEC Cooperative Research Projects (S.K., S.F. and H.O.).

Author contributions

S.F. and H.O. planned the study. S.K. and T.F. designed the experiment and analysis. T.F. prepared samples, performed measurements and analysed the data under the support of S.K. S.K. formulated the bifurcation of the dynamics of nanomagnet. S.K. and S.F. wrote the manuscript with input from H.O. and J.I. All authors discussed the results.

Competing interests

The authors declare no competing interests.

Additional information

Supplementary information The online version contains supplementary material available at <https://doi.org/10.1038/s41467-022-31788-1>.

Correspondence and requests for materials should be addressed to Shun Kanai or Shunsuke Fukami.

Peer review information *Nature Communications* thanks Jian-Ping Wang and the other, anonymous, reviewer(s) for their contribution to the peer review of this work.

Reprints and permission information is available at <http://www.nature.com/reprints>

Publisher's note Springer Nature remains neutral with regard to jurisdictional claims in published maps and institutional affiliations.



Open Access This article is licensed under a Creative Commons Attribution 4.0 International License, which permits use, sharing, adaptation, distribution and reproduction in any medium or format, as long as you give appropriate credit to the original author(s) and the source, provide a link to the Creative Commons license, and indicate if changes were made. The images or other third party material in this article are included in the article's Creative Commons license, unless indicated otherwise in a credit line to the material. If material is not included in the article's Creative Commons license and your intended use is not permitted by statutory regulation or exceeds the permitted use, you will need to obtain permission directly from the copyright holder. To view a copy of this license, visit <http://creativecommons.org/licenses/by/4.0/>.

© The Author(s) 2022